Dynamic and equilibrium properties of finite-size polymer models of chromosome folding

Mattia Conte,[1,*] Luca Fiorillo,[1] Carlo Annunziatella,[1] Andrea Esposito,[1] Francesco Musella,[1] Alex Abraham,[1] Simona Bianco,[2,†] and Andrea M. Chiariello[1,‡]

[1]*Dipartimento di Fisica, Università di Napoli Federico II, and INFN Napoli, Complesso Universitario di Monte Sant'Angelo, 80126 Naples, Italy*

[2]*Berlin Institute for Medical Systems Biology, Max-Delbrück Center (MDC) for Molecular Medicine, Hannoversche Str. 28, 10115, Berlin, Germany*

(Received 4 May 2021; accepted 12 October 2021; published 10 November 2021)

Novel technologies are revealing that chromosomes have a complex three-dimensional organization within the cell nucleus that serves functional purposes. Models from polymer physics have been developed to quantitively understand the molecular principles controlling their structure and folding mechanisms. Here, by using massive molecular-dynamics simulations we show that classical scaling laws combined with finite-size effects of a simple polymer model can effectively explain the scaling behavior that chromatin exhibits at the topologically associating domains level, as revealed by experimental observations. Model results are then validated against recently published high-resolution *in situ* Hi-C data.

DOI: 10.1103/PhysRevE.104.054402

I. INTRODUCTION

Within the cell nucleus, chromosomes are folded into a complex, nonrandom, multiscale three-dimensional (3D) architecture [1–5]. Such a spatial organization serves important functional purposes as, for instance, gene expression is regulated via the formation of chromatin loops between regulatory elements and their target genes. Also, alterations of chromatin folding have been linked to congenital diseases [6,7]. Novel technologies, such as Hi-C [8], genome architecture mapping (GAM) [9], and split-pool recognition of interactions by tag extension (SPRITE) [10], have shown that chromosomes are highly compartmentalized, forming a hierarchy of multiple genomic interactions ranging from loops [11] and topologically associating domains (TADs) [12,13] to, above the mega-base scale, metaTADs [14], A/B compartments [8], and lamina-based domains [15]. Also, different chromosomes in turn interact [11] and form a nonrandom network of contacts [16]. On the other hand, recent single-cell Hi-C [17–20] and super-resolution multiplexed-fluorescence *in situ* hybridization (FISH) imaging experiments [21–24] have revealed that chromatin interactions are highly stochastic and contact domains broadly vary from cell to cell.

To understand the molecular mechanisms underlying the complex spatial organization of chromosomes, different polymer models and computational methods have been developed [25–34]. Here, we consider the textbook scenario envisaged by the strings and binders switch (SBS) model [30,31], where diffusible DNA-binding molecules establish chromatin loops via thermodynamics mechanisms by bridging distal polymer sites. The SBS model has been shown to explain key properties of chromosome large-scale 3D organization [35] as well as the folding of specific genomic loci [36] at the single-molecule level [37], and also to predict *in silico* the effects of pathogenic structural variants [38].

Here, by use of massive molecular-dynamics (MD) simulations at different polymer lengths we investigate the effect of the system size on relevant dynamic and equilibrium properties of the model. First, we focus on the folding dynamics and find that the polymer self-assembly time, i.e., the time required to fold an initial coil (i.e., randomly folded) conformation into an equilibrium globule, exhibits a nontrivial scaling law that can be mechanistically linked to the SBS interaction process between polymer binding sites and binders. Next, we study size effects on our equilibrium, globulelike, polymer conformations, focusing on the average pairwise contact probability, $P_c(s)$, of polymer sites at a given contour distance s. Measurements of $P_c(s)$ from Hi-C experiments have revealed a power-law behavior at genomic distances at least within the range 0.5–7 Mb, $P_c(s) \sim s^{\gamma}$ ($\gamma < 0$) [8], with an average exponent $\gamma \approx -0.75$ inside individual contact domains [25]. It has been also shown that γ is not conserved across different systems and chromosomes [31,39–43], pointing out that a single universal architecture, described, e.g., by the attractive "fractal-globule" polymer model [44,45], poorly describes genome folding [31,46,47]. Here, we show that the exponent γ depends on the size of the simulated polymer conformations and it decreases upon increase of the polymer length. Our results are then compared against recent ultradeep *in situ* Hi-C data in mouse neural differentiation [48], where we compute γ inside individual contact domains in different cell types. Intriguingly, we find that the experimental contact probability exponent scales with the genomic size of the domains as predicted by our physical simulations. Overall, our data indicate that the observed variability of γ exponents at the TAD level can be explained by basic concepts of polymer physics.

*mattia.conte@na.infn.it
†simona.bianco@mdc-berlin.de
‡chiariello@na.infn.it

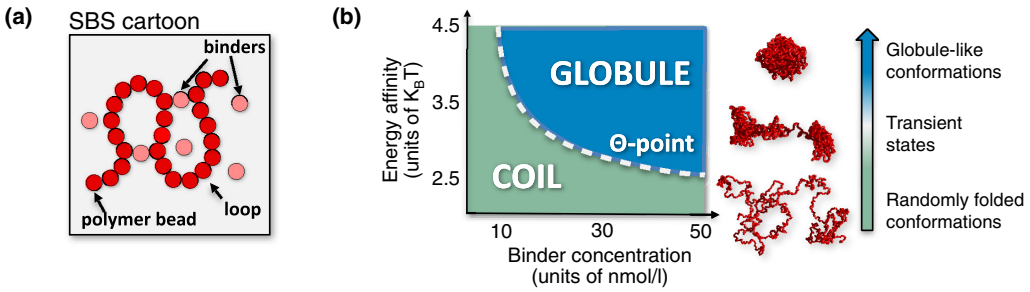

FIG. 1. (a) Cartoon of the SBS polymer model. Diffusing molecular binders bring distal polymer sites into close spatial proximity, thus looping the chain. (b) According to the binder concentration or affinity, two main thermodynamics phases of the model are established: the coil state, where the polymer folds into randomly open conformations belonging to the universality class of the free SAW [49], and the globule state, where the system spontaneously collapses, above the Θ line, into a compact closed conformation. Polymer 3D configurations with $N = 1000$ beads.

II. MODEL AND SIMULATION DETAILS

A. The model

In the SBS model, a chromatin filament is represented as a self-avoiding walk (SAW) polymer chain having binding sites for diffusing cognate binders, which can form loops by bridging together pairs of polymer sites [30,31,35] [Fig. 1(a)]. According to the concentration and/or interaction affinity of binders, the system undergoes a phase transition from an initial coil state, where entropic forces fold the polymer into random open conformations, to an equilibrium globule state, where the system shrinks in closed globular conformations due to attractive interactions. As dictated by polymer physics [49], all system 3D conformations fall in those two main folding classes corresponding to its thermodynamics phases. A phase transition line, corresponding to the Θ point, marks the boundary between the two phases [Fig. 1(b)].

B. MD simulations

In this study, we focus on the simplest case of SBS polymer models, i.e., homopolymer chains where all beads are identical and interact with only one type of binder. Despite their simplicity, toy homopolymer models have been used to understand large-scale features of chromatin folding [31,35] and indeed provide a good proxy to study average properties, e.g., contact probabilities, within individual globular contact domains.

We perform massive MD simulations of SBS homopolymers at different lengths, considering systems made of $N =$ 100, 200, 500, 1000, 2000, and 5000 monomers. We use standard interaction potentials developed in classical polymer physics studies [50] and set all details of computer simulations as in Refs. [35,37]. Briefly, we model: (i) the hard-core repulsion between two adjacent polymer sites using the Weeks-Chandler-Andersen (WCA) potential:

$$V_{WCA}(r) = 4\varepsilon\left[\left(\frac{\sigma}{r}\right)^{12} - \left(\frac{\sigma}{r}\right)^{6} + \frac{1}{4}\right], \qquad (1)$$

where $\varepsilon = K_BT$ is the energy unit (K_B is the Boltzmann constant and T is the temperature), σ is the bead diameter, and r is the distance between two particle centers ($V_{WCA} = 0$ if $r > 2^{1/6}\sigma$); (ii) the attractive bond between consecutive monomers of the chain by a finitely extensible nonlinear elastic (FENE) potential with standard parameters [50]:

$$V_{\mathrm{FENE}}(r) = -\frac{1}{2}k\left(\frac{R_0}{\sigma}\right)^2 \ln\left[1 - \left(\frac{r}{\sigma}\right)^2\right], \qquad (2)$$

where k is the strength of the FENE spring and R_0 is its maximal extension, i.e., the maximal length of the bond ($V_{\mathrm{FENE}} = \infty$ if $r > R_0$); and (iii) the interaction between polymer sites and binders by a short-ranged, attractive Lennard-Jones (LJ) potential [27]:

$$V_{LJ}(r) = 4\varepsilon_{\mathrm{int}}\left[\left(\frac{\sigma_{bb}}{r}\right)^{12} - \left(\frac{\sigma_{bb}}{r}\right)^{6} - \left(\frac{\sigma_{bb}}{r_{\mathrm{int}}}\right)^{12} + \left(\frac{\sigma_{bb}}{r_{\mathrm{int}}}\right)^{6}\right], \qquad (3)$$

where σ_{bb} is the sum of bead and binder radii, $\varepsilon_{\mathrm{int}}$ is the control parameter for the intensity of the polymer-binder interaction, r is the bead-binder center-to-center distance and r_{int} is the cutoff distance value that sets the interaction range ($V_{LJ} = 0$ if $r \geqslant r_{\mathrm{int}}$). For simplicity, polymer beads and binders have the same diameter, σ.

The polymer system is subject to the Langevin equation:

$$m\frac{d^2}{dt^2}\boldsymbol{x}(t) = -\zeta\frac{d}{dt}\boldsymbol{x}(t) - \nabla U(\boldsymbol{x}(t)) + \boldsymbol{\xi}(t), \qquad (4)$$

where $\boldsymbol{x}(t)$ is the 3D vector of the particle coordinates, m is the mass of the particle, ζ its friction coefficient in the solvent, U is the total potential acting on the particle, i.e., the superposition of (1), (2), and (3), and $\boldsymbol{\xi}(t)$ the randomly fluctuating force. The equation is numerically solved using the velocity-Verlet algorithm within the LAMMPS software [51] and parameters are set as in Ref. [35].

The system evolves up to 10^8 MD timesteps when stationarity is reached (see next section). To remove boundary effects, we impose periodic conditions in the simulation box. We sample in our simulations a spectrum of binding energy affinities in the weak biochemical energy range, from 2.7 to $4.0K_BT$, which ensure the coil-globule transition for binder concentrations falling in the fractions of μmol/l range [35,37], values compatible with the nuclear concentrations of transcription factors. For each considered number of monomers N, we produce a thermodynamics ensemble of 200 independent polymer conformations.

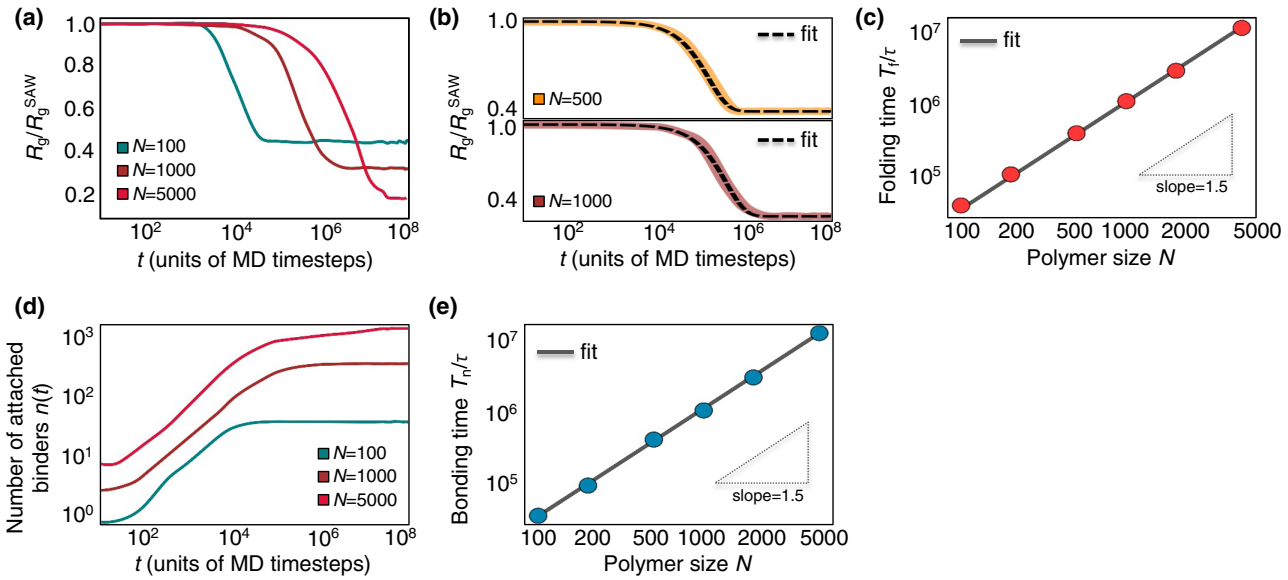

FIG. 2. (a) Polymer gyration radius, R_g, averaged over the ensemble of polymer conformations and normalized by its SAW value as a function of the MD simulation timesteps (logarithmic x scale). Three cases shown with $N = 100$, 1000, and 5000 monomers. Its sharp decrease signals the transition of the system from the initial coil state to the equilibrium globule phase. (b) Exponential fit of gyration radius vs time (MD units), logarithmic x scale. Two examples are shown with $N = 500$, 1000 ($\chi^2 < e{-}2$, chi-squared test). (c) The polymer folding time T_f, i.e., the time to fold the initial free SAW polymer chain into an equilibrium globule, scales as a power law of the system size, $T_f \sim N^{1.5}$, where the exponent is the slope of the best-fit line on log-log axes (r-squared $r^2 = 0.99$; statistical errors <5% and contained within the point size). Time values on y axis are in MD units, τ being the time unit. (d) Time dynamics of the number of binders, $n(t)$, progressively attached to the polymer binding sites during the simulation. Three cases plotted with $N = 100$, 1000, and 5000. (e) The bonding time, measured by exponential fit of $n(t)$, scales as $N^{1.5}$ (log-log axes, MD units, $r^2 = 0.99$), i.e., with the same exponent of the polymer folding time. Hence, the dynamics of diffusible DNA-binding molecules affects the polymer folding time in a size-dependent manner.

III. RESULTS

A. Polymer folding dynamics

The initial states of our MD simulations are distinct SAW conformations, prepared as described in Ref. [50]. Then, the binders are randomly introduced within the simulation box and interact with the polymer beads [35,37]. To monitor the system dynamics, we observed the time course of the gyration radius of the polymer chain, R_g [49,52]. The sharp decrease of R_g as function of the time (expressed as MD time iteration steps) signals the phase transition of the system from the initial coil state (high R_g), to an equilibrium folded state in which R_g takes lower values and plateaus [Fig. 2(a); three cases with $N = 100$, 1000, and 5000 are shown]. A similar dynamical behavior is observed for the total potential energy (i.e., the bead-bead FENE and the bead-binder LJ interactions) [37].

As expected, shorter polymers reach earlier the plateauing of R_g, whereas a larger time ($>10^6$ MD timesteps) is required for longer polymers. To quantitatively investigate how the system size affects the polymer self-assembly folding time, we fitted the gyration radius using the function $g(t) = ae^{-bt} + c$ [Fig. 2(b); two examples with $N = 500$, 1000. $\chi^2 < e{-}2$, chi-squared test). The folding time, T_f, is then defined as the ratio $3/b$, since at this time the fit function spans nearly 95% of its y range, and we found that T_f increases with the system size as $N^{1.5}$ [Fig. 2(c); r-squared $r^2 = 0.99$; τ is the MD time unit). By comparing this exponent with textbook results of polymer physics [52], we noticed, for instance, that it is lower than the relaxation time of the Rouse chain ($\sim N^2$), where polymer dynamics is governed by the Brownian motion and excluded volume effects are not considered. Similarly, this exponent also differs from the usual reptation time, as the formation of the entangled equilibrium globule is a diffusive, very slow process with equilibration time $\sim N^3$ [44,45]. Conversely, the model exponent turns out to be consistent with the relaxation time of the Zimm model, which includes solvent-mediated hydrodynamic interactions between different parts of the chain [52]. Thus, we reasoned that the scaling time behavior observed in our model traces back to presence of the binders, as they drive the folding by bridging distal polymer sites.

To provide a mechanistic understanding of such exponent, we considered the number of binders, $n(t)$, that progressively attach to the polymer chain during the folding process [Fig. 2(d); three cases with $N = 100$, 1000, and 5000 shown]. The function $n(t)$, differently from R_g, increases in time until stationarity is reached, as the polymer needs in its folding dynamics a growing number of binders to stably loop the chain into an equilibrium globule conformation. Also, $n(t)$ is affected by the system size, because shorter polymers require fewer binders to achieve thermodynamics equilibrium than longer polymers, as shown, e.g., in Fig. 2(d), where the plateau level of $n(t)$ differs by a factor 10^2 when the polymer length switches from 100 to 5000 monomers. As before, we

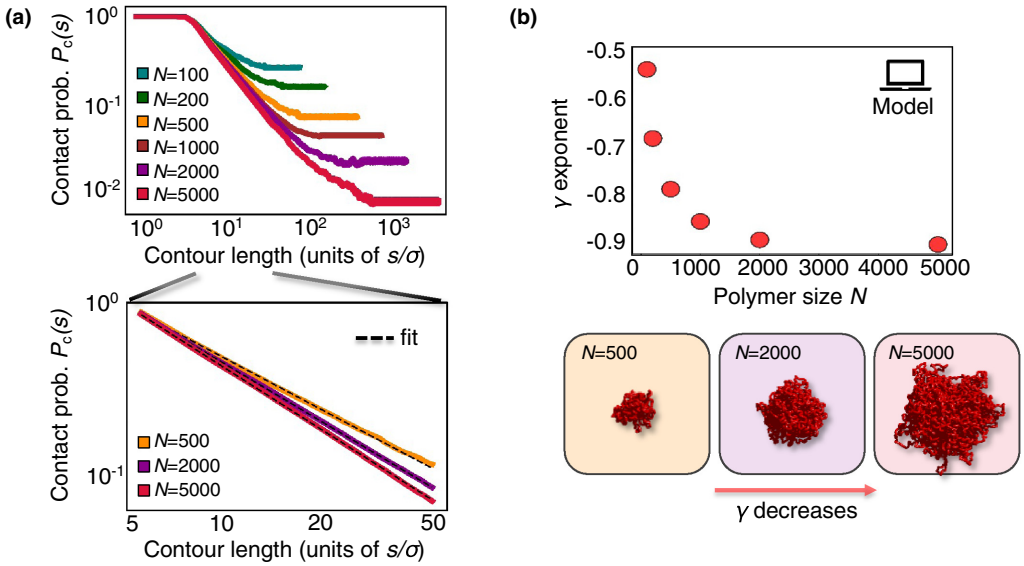

FIG. 3. (a) Top: double-logarithmic plot, at different polymer lengths N, of the average pairwise contact probability of the model, P_c, as a function of the polymer contour length, s, in the equilibrium globule phase (MD units, σ is the model length scale). For each N, the contact probability decays with s and reaches a plateau at large contour distance. Bottom: zoom of $P_c(s)$ at intermediate contour lengths, where the function scales as a power law (i.e., straight line on log-log axes). The contact probability exponent γ, measured as the slope of its best-fit line in that region, becomes smaller as N increases and thus depends on the polymer size. Three examples are shown with $N = 500$, 2000, and 5000. (b) Top: the model-derived contact probability exponent, γ, is plotted against the polymer size. The exponent decays as a function of N, spanning a range of values from -0.55 to -0.90. Statistical errors $<2\%$ and confined within the point size. Bottom: 3D snapshots of equilibrium globule conformations at different polymer lengths. The exponent γ decreases with the system size, thus hinting that its observed biological variability can be recapitulated by basic scaling concepts of polymer physics.

used an exponential function to fit $n(t)$ and defined the bonding time, T_n, as the time required to reach 95% of its y range. We found, as expected, that the bonding time is well described by $T_n \sim N^{1.5}$ [Fig. 2(e), $r^2 = 0.99$], i.e., by the same power law of the gyration radius $R_g(t)$. This result suggests that the binding process of molecules directly influences the polymer folding time in a size-dependent manner and provides a mechanistic rationale of the time exponent of the model.

To give a sense of the physical times involved, by taking, for instance, a reference time unit of a few milliseconds (e.g., 20 ms) [27,35,53,54], the power-law relation found provides that the self-assembly time of a chromatin filament lies in the typical temporal scales of biological processes**,** ranging from seconds to hours [27,35,54]. The folding dynamics envisaged by the SBS model, driven by diffusing molecular particles that mediate chromatin long-range interactions, is consistent with the emerging biological picture where cooperative multimolecular assemblies, such as combinations of RNA polymerase II with transcription factors and cofactors, as the Mediator complex, control gene activity by the formation of functionally relevant, phase-separated, chromatin hubs [55–59].

B. Contact probability scaling exponent depends on the polymer size

Next, we investigated the effects of the system size on equilibrium properties of the model in its globule phase. We focused on the average pairwise contact probability, $P_c(s)$, which can be accessed by Hi-C experiments and measures how frequently two chromatin loci contact each other as a function of their genomic linear distance s. From our simulations, $P_c(s)$ is easily computed by setting a distance threshold $M\sigma$, where M is a positive number, that defines two polymer beads in contact [35,38]. We set $M = 3.5$ in our simulations, but we also checked that different values of M return similar results [60]. For each value of the polymer length N, $P_c(s)$ is averaged across the ensemble of single-molecule conformations. Importantly, as dictated by polymer physics [49], the contact probabilities computed in the equilibrium globule state do not depend on the model finer details, such as the exact value of the binder concentration or energy affinity [see Appendix B, Fig. 6(a)].

The model contact probability derived from our simulation monotonically decays for every N with the polymer contour length s (i.e., the genomic separation if mapped onto genomic coordinates) until a plateau, P_∞, is approached [Fig. 3(a), top]. As expected from the globular topology of the chain, such a plateau decreases as N grows and scales with the polymer length as $N^{-0.9}$ (Appendix A). At short and intermediate contour distances the behavior of the contact probability is more complex, as measurements of $P_c(s)$ from Hi-C data have identified in the genomic region 0.5–7 Mb a power-law behavior, $P_c(s) \sim s^\gamma$ ($\gamma < 0$) [8]. The scaling exponent γ can be thus measured as the slope of the best-fit line on $P_c(s)$ when plotted on log-log axes, as shown for our simulations in Fig. 3(a) (bottom, zoom within the linear fitted region, three examples with $N = 500$, 2000, and 5000). We fitted the contact probabilities within a range of distances $[s_0, s^*]$, with $s_0 = 5\sigma$ and s^* satisfying $P_c(s^*) = 1-0.95(1 - P_\infty)$, avoiding in this way boundary effects in the computation of γ. We also checked that different choices of s^* within the power-law

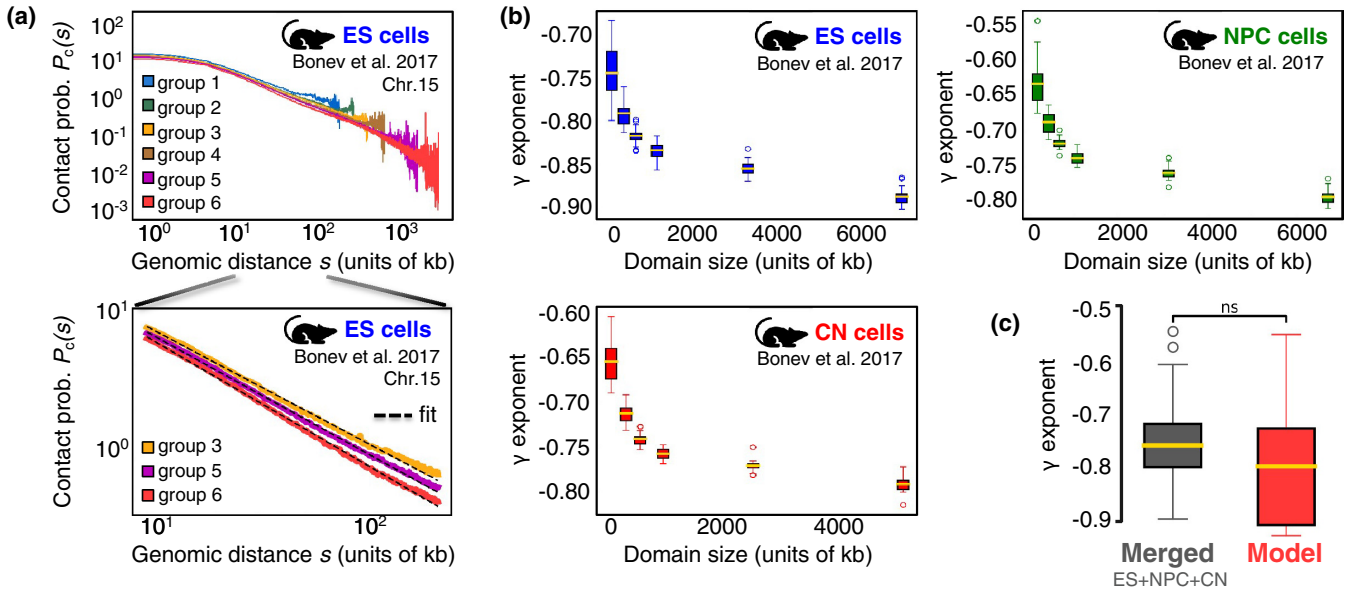

FIG. 4. (a) Top: average pairwise contact probability $P_c(s)$ of chromosome 15 in ES cells within each identified group of domain sizes from Ref. [48]. The function decays with the genomic distance (expressed in kilobase pairs, kb) and scales as power law at intermediate distances (linear segment on log-log axes). Bottom: zoom of the intermediate power-law region in the range 10–200 kb. The slope of the best-fit line on $P_c(s)$, γ, depends on the group of contact domains, as it declines with their size. (b) Boxplots reporting the genomewide distribution of γ exponents for each group of domains. Results are shown for ES (top left, in blue), NPC (top right, in green), and CN cells (bottom, in red). In all three cell types, the contact probability scaling exponent γ decreases with the domain size, as found in our physical simulations. The boxes extend from the lower to upper quartile values of the data, with mean highlighted in yellow. The x value of each box is the average size of the corresponding group of domains. The y axis is different in the different cell lines to better highlight the cell-type specific range and scaling of the contact exponents. (c) The overall experimental range of γ values within all groups of domains, computed across all chromosomes and cell types ("merged" in our notation), is similar to that derived in our model by varying the polymer length ($p = 0.55$, Welch's t test), showing that simple size scaling effects of polymer physics can recapitulate the observed variability of exponents emerging from the experiments.

regime do not change our results [see Appendix B, Fig. 6(b)]. Interestingly, we found that γ is affected by the polymer size and decreases as N grows, spanning a range from -0.55 to -0.90 [Fig. 3(b), top; a summary cartoon is sketched below with 3D polymer snapshots at different lengths). Notably, this range is consistent with the experimental variability of γ detected within contact domains across different human cell types [11], where an average value $\gamma \approx -0.75$ is observed [25]. To further assess the robustness of our results, we also computed with a similar procedure the scaling exponents of the mean-square spatial distance at the small contour length regime. Consistently, we found that those exponents span the same range of values derived for γ, albeit they increase with the system size as contacts and distances are inversely related [61,62] [see Appendix B, Fig. 6(c)].

Overall, our results indicate that the contact probability exponent γ depends on the system size, thus hinting that finite-size effects can recapitulate its biological range of variability.

C. Model scaling is validated against high-resolution Hi-C data

To test the dependence of γ on the system size in real cells, we computed the contact probability scaling exponent within topological domains using recently published ultradeep *in situ* Hi-C data [48], which are available at high resolution (1 kb) across different cell lines in mouse embryonic stem (ES) cells, neural progenitors (NPC), and cortical neurons (CN). First, in order to identify a discrete number of domain sizes for each cell line, we clustered the contact domains from Ref. [48] into six, cell-type-specific groups based on their genomic length [see Appendix C, Figs. 7(a) and 7(b)]. Then, we computed the average contact probability $P_c(s)$ of each chromosome within each identified group and derived the corresponding value of the scaling exponent γ in that group. That allowed us to quantitively investigate how the size of the contact domains affects the value of γ.

As an example, we reported in Fig. 4(a) (top) the $P_c(s)$ of chromosome 15 in ES cells computed within our six different groups of domains. The function decays, as expected, with the genomic separation and exhibits in all groups a power-law behavior (linear segment on log-log axes) at intermediate distances, roughly in the genomic distance range 10–200 kb. Interestingly, this range is consistent with our simulations [Fig. 3(a), bottom], once the dimensionless MD units of the models are mapped into genomic base pairs by using standard mapping coefficients expressing the genomic content of the polymer bead, which are typically in the range 1–10 kb [31,54,63]. Hence, we fitted the Hi-C contact probability in the power-law regime and derived the experimental γ [Fig. 4(a), bottom; zoom of the fitted region for three different groups of domains]. Notably, the scaling exponent γ depends on the considered group, i.e., on the size of the contact domains and decreases as the average domain size increases. We also implemented the same procedure on chromosome 15 in NPC and CN cells and observed an analogous behavior of the

scaling exponent [see Appendix C, Fig. 7(c)]. Similar results are then found in other individual chromosomes.

Next, we extended our analysis on Hi-C data genomewide, considering for each cell type and group of domains the distribution of γ exponents from all chromosomes [boxplots in Fig. 4(b) for ES (blue), NPC (green), and CN (red) cells; sexual chromosomes excluded]. Interestingly, γ monotonically decays in the different cell lines as a function of the domain size, with its mean value decreasing by about 20% moving from the first to the last group of domains. Hence, γ depends on the size of the contact domains as predicted by the model and its range of values, for all the three cell types considered, is consistent with the range of our polymer simulations. Indeed, to estimate the overall experimental variability of γ during cell differentiation, we computed the genomewide distribution of exponents from all groups of domains and cell types and found that it significantly matches the cumulative range of γ values (from -0.55 to -0.90) derived by our simulations at different polymer lengths [Fig. 4(c), $p = 0.55$, Welch's t test].

Taken together, our analyses show that size scaling effects observed in a simple, classical polymer physics model can reliably capture the variability of contact probability exponents observed in the experiments.

IV. CONCLUSIONS

Models combining polymer physics and computational methods are now an essential tool to quantitatively investigate chromosome spatial organization. In this work, we focused on the classical scenario where diffusing binding molecules can establish and dynamically change, by switchlike thermodynamics mechanisms, polymer architectural patterns, as described by the SBS model [30,31]. Upon increasing binder concentration or binding affinity, the polymer model undergoes a phase transition from an initial coil, i.e., randomly folded, to an equilibrium globule state [35,37].

Here, by performing massive molecular-dynamics simulations, we investigated how dynamic and equilibrium properties of the model are affected by the system size. We found that the characteristic time of the coil-to-globule transition increases as power law of the polymer length, with a scaling exponent 1.5 lower than expected from classical reptation models of polymer physics [52]. Such time behavior results from the physical mechanism underlying the self-assembly of polymer conformations in the SBS model, where molecular binders fold the chain into equilibrium globule conformations by bridging together distal polymer sites. The binder-driven mechanism of chromatin folding envisaged by the model is consistent with recent experiments where regulatory proteins, e.g., transcription factors, and biomolecular phase-separated condensates have been shown to compartmentalize biochemical reactions within cells and control gene expression via cooperative interactions [55,56,59,64,65].

Finally, we studied the effects of the polymer size on equilibrium properties of the model, focusing on the contact probability $P_c(s)$. We showed that its scaling exponent γ is affected by the polymer length, as it decays with the polymer size. To validate model results, we performed a genomewide analysis of contact probabilities within topological domains using recent high-resolution *in situ* Hi-C data from Ref. [48] in mouse neural differentiation. Importantly, we found that the experimental γ depends on the genomic length of the contact domains and decays with their size as predicted by our physical simulations. Also, the overall experimental variability of γ during neural differentiation significantly matches the range of exponents derived by the model. Remarkably, such a variability spontaneously emerges from a simple scaling analysis of finite-size polymer simulations, without any additional fine-tuning of system parameters.

In this work we considered a basic homopolymer toy model as a first approximation to study the contact probabilities within TADs of different domain sizes. However, TADs are not isolated domains, as they are involved in higher-order interactions extending across genomic scales up to the range of entire chromosomes [14]. Therefore, more sophisticated polymer models, such as interacting block copolymers or active mechanisms, could further improve the agreement between simulations and experiments. Despite the basic ingredients of the models employed here, our results indicate, overall, that basic concepts from polymer physics and finite-size effects can recapitulate the observed scaling behavior of chromatin within contact domains.

ACKNOWLEDGMENTS

A.M.C. acknowledges financial support from "*Programma per il Finanziamento della Ricerca di Ateneo Linea B'* (FRA) 2020, University of Naples Federico II. S.B. and A.M.C. acknowledge support from the CINECA ISCRA Grant ID No. HP10CCZ4KN. The authors acknowledge computer resources from INFN, ENEA CRESCO/ENEAGRID [66], and *Scope/ReCAS/Ibisco* at the University of Naples.

A.M.C. and M.C. conceived the project; A.M.C. and S.B. supervised the project; M.C. performed and analyzed numerical simulations; M.C., A.E., L.F., and C.A. analyzed chromatin data; and A.M.C., M.C., and S.B. wrote the manuscript with input from all authors.

APPENDIX A: EQUILIBRIUM GLOBULE PHASE OF THE MODEL

The plateau of $P_c(s)$, P_∞, is expected to scale as $N^{-0.9}$ in the equilibrium globule phase of the model. Such a behavior can be easily assessed as follows. For every N, we computed the average pairwise squared Euclidean distance, R^2, of polymer sites at a given contour distance s. The function $R^2(s)$, which can be accessed by FISH experiments, increases with the genomic separation up to plateauing [Fig. 5(a), left]. The plateau value of R^2, R^2_∞, scales as $N^{0.6}$ consistent with the globular topology of our polymer conformations [Fig. 5(a), right]. Thus, by taking contacts proportional to the inverse of the volume V occupied by the polymer, we have $P_\infty \sim V^{-1} \sim (R_\infty)^{-3} \sim N^{-0.9}$, as indeed shown in Fig. 5(b).

APPENDIX B: ROBUSTNESS OF THE MODEL-DERIVED CONTACT EXPONENTS

To test here the statistical robustness of the model contact exponents discussed in Sec. III B, we first checked that

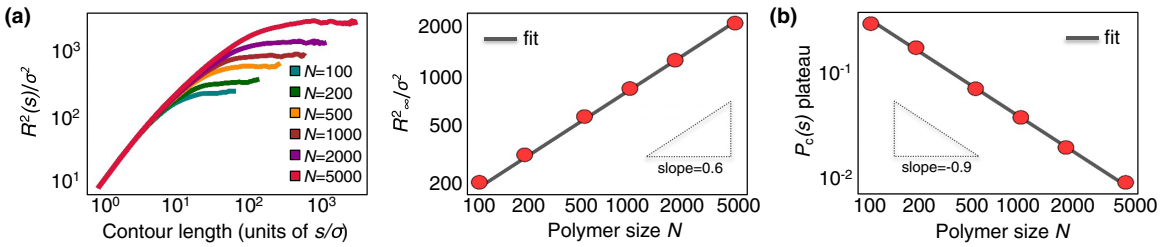

FIG. 5. (a) Left: average pairwise Euclidean distance, $R^2(s)$, as a function of the contour length at different polymer sizes (log-log axes, MD units). Right: R^2 plateau, R^2_∞, scales as $N^{0.6}$, as expected because the equilibrium chain is globulelike. (b) Double-logarithmic plot showing the plateau of $P_c(s)$ as a function of the polymer size N. It scales as $N^{-0.9}$ in the equilibrium globule phase of the model.

different binder concentrations in the equilibrium globule phase do provide, as expected from polymer physics [49], the same contact exponents. Precisely, the molar concentration of binders is $c = P/VN_A$, where N_A is the Avogadro number, V is the simulation box volume, and P is the number of binders in the box. In all our simulations we set $P = 0.5N$, which provides binder concentrations high enough such that the polymer is in the completely globule state [35]. However, changes around this reference value do not affect the contact probabilities. Indeed, in Fig. 6(a) (left panel) we reported the contact probability as a function of the genomic distance for $N = 1000$ by using different concentration values in the equilibrium globule phase, i.e., 20% higher (dark brown, $P = 0.6N$) and lower (orange, $P = 0.4N$) than the value used in the main text (brown, $P = 0.5N$). As expected, the curves collapse all on the top of each other ($\chi^2 < e-2$, chi-squared test) and, importantly, they provide the same contact exponent [Fig. 6(a), right panel; the relative error in the estimation of the exponent is less than 2%].

Next, we checked whether the contact exponents derived from the model sensitively depend on the power-law region used in the fit (i.e., on different choices of s^*). To that aim, we computed the contact probability exponents by varying s^* in a wide range within the $P_c(s)$ power-law regions of the models [Fig. 6(b); two cases shown with $N = 1000$ and $N = 5000$]. Our analysis shows that the values of the exponent γ upon changing s^* are all consistent with each other within the statistical errors and do not depend on this parameter. In particular, for a given N, the value of γ averaged over the different choices of s^* differs less than 1% from the exponents reported in Fig. 3(b) [Fig. 6(b)].

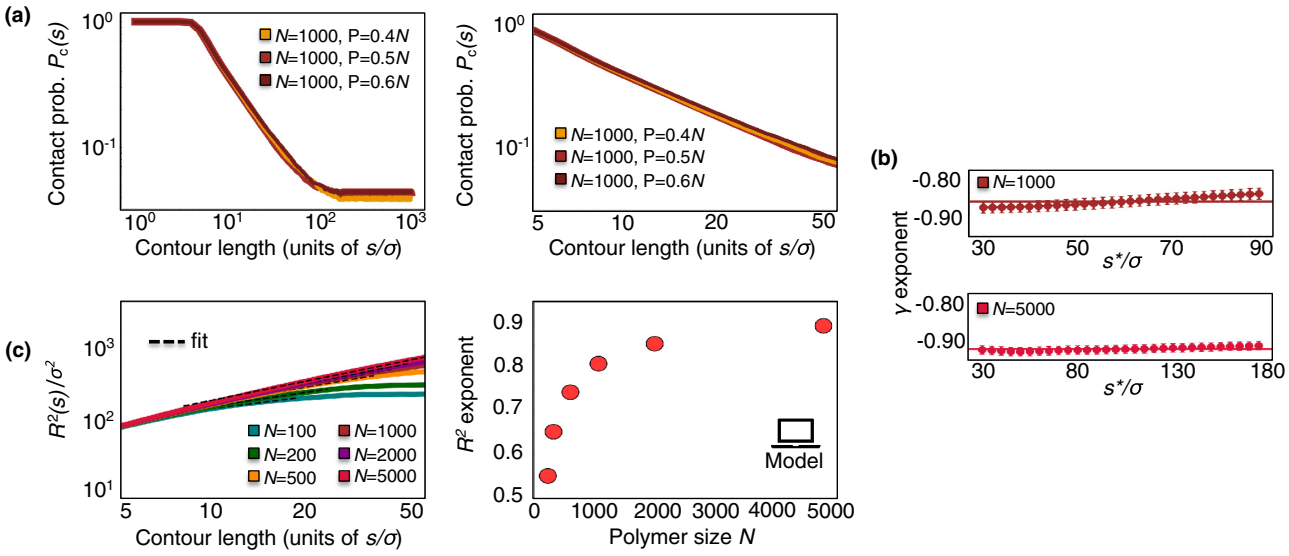

FIG. 6. (a) The equilibrium properties of the system, such as the contact probability, do not depend on the exact value of the binder concentration in the thermodynamics equilibrium globule phase. Left panel: contact probability as a function of the genomic distance for $N = 1000$ by using different concentration values in the equilibrium globule state, i.e., 20% higher (dark brown, $P = 0.6N$) and lower (orange, $P = 0.4N$) than the value used in the text (brown, $P = 0.5N$). As expected, the curves collapse all on the top of each other. Right panel: the contact probabilities at different binder concentrations provide all the same γ exponent (relative error less than 2%). (b) The estimation of the γ exponent is robust in the power-law region $[s_0, s^*]$ upon change of the parameter s^*. Two cases shown here with $N = 1000$ (top) and $N = 5000$ (bottom). Error bar is the fit statistical error. The horizontal line is the average γ computed over the different values of s^* reported in the plots. The average differs less than 1% from the exponents of Fig. 3(b), thus ensuring that different choices of s^* within the $P_c(s)$ power-law regime do not affect the results. (c) Left panel: the average squared distance, $R^2(s)$, exhibits at short contour lengths s a power-law scaling for each of the considered polymer lengths. Right panel: R^2 exponents depend on the polymer size and have a similar, yet opposite, trend with respect to the contact exponents γ.

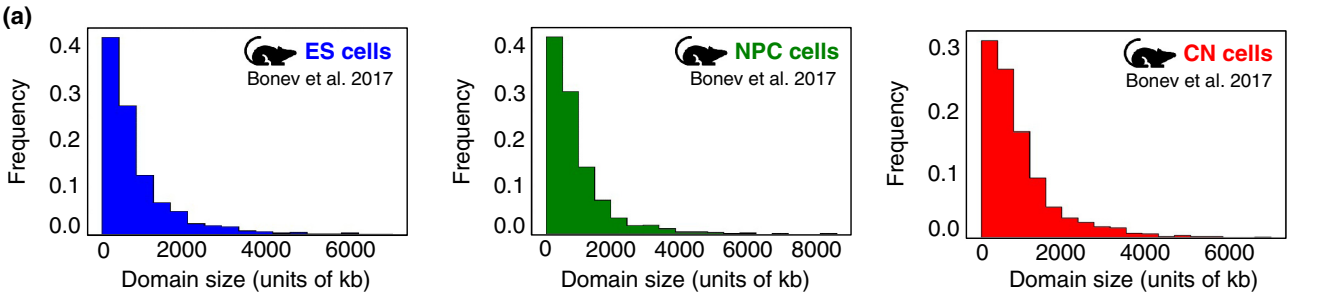

(b)

	ES	NPC	CN
group 1	0.00-0.26Mb	0.00-0.31Mb	0.00-0.32Mb
group 2	0.26-0.45Mb	0.31-0.51Mb	0.32-0.53Mb
group 3	0.45-0.71Mb	0.51-0.79Mb	0.53-0.82Mb
group 4	0.71-1.24Mb	0.79-1.32Mb	0.82-1.35Mb
group 5	1.24-4.11Mb	1.32-4.91Mb	1.35-4.05Mb
group 6	4.11-6.98Mb	4.91-8.51Mb	4.05-6.74Mb

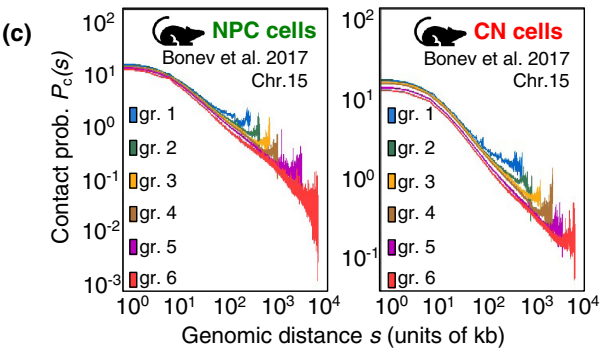

FIG. 7. (a) Genomewide distribution of the size of contact domains at 1-kb resolution from Ref. [48]. Sexual chromosomes are excluded in our analyses. Results are shown for ES (left, in blue), NPC (middle, in green), and CN (right, in red) cells. (b) Summary table reporting the size range of contact domains falling within each identified group. (c) Pairwise contact probability, $P_c(s)$, of chromosome 15 in NPC (left, in green) and CN cells (right, in red) computed within our identified groups of domains from Ref. [48].

Finally, we computed, as with Fig. 3(a), the scaling exponents of the mean-squared distances, $R^2(s)$, reported in Fig. 5(a). At the small contour length regime, the functions $R^2(s)$ exhibit a power-law behavior for each of the considered polymer lengths [Fig. 6(c), left]. The scaling exponents depend on the polymer size, N, and return the same range of values derived for γ, albeit they increase with the system size as contacts and distances are inversely related [Fig. 6(c), right]. That finding strengthens our results, i.e., opposite trend.

APPENDIX C: Hi-C TOPOLOGICAL DOMAINS ARE GROUPED BASED ON THEIR SIZE

We clustered the contact domains reported in Ref. [48] based on their genomic length. By using the genomic coordinates identifying topologically associating domains in Ref. [48], we derived the genomewide distribution of domain sizes in ES, NPC, and CN cells [histograms shown in Fig. 7(a); sexual chromosomes excluded in our analyses]. Then, in order to group domains according to their size, we initially split the distributions of domain sizes into quintiles, as this choice provides a robust statistical ensemble (500 domains on average falling within each group). However, as the last quintile of the distributions is related to multiple larger domains spanning from 1 Mb to more than 7 Mb, we further divided it in two equal parts to avoid underestimating γ in that group. Based on this procedure, we identified overall six, cell-type-specific clusters of domain sizes [see Table in Fig. 7(b)], referred to in the text and figures as group 1–6. For a given chromosome, we computed the average contact probability $P_c(s)$ within each group and thus the corresponding value of the scaling exponent γ in that group. In Fig. 7(c), we reported, as additional examples, the contact probabilities of chromosome 15 in NPC and CN cells within the identified groups of domains.

[1] T. Cremer and C. Cremer, Chromosometerritories, nuclear architecture and gene regulation in mammalian cells, Nat. Rev. Genet. **2**, 292 (2001).

[2] T. Misteli, Beyond the sequence: Cellular organization of genome function, Cell **128**, 787 (2007).

[3] J. Dekker and L. Mirny, The 3D genome as moderator of chromosomal communication, Cell **164**, 1110 (2016).

[4] W. A. Bickmore and B. Van Steensel, Genome architecture: domain organization of interphase chromosomes, Cell **152**, 1270 (2013).

[5] J. R. Dixon, D. U. Gorkin, and B. Ren, Chromatin domains: The unit of chromosome organization, Mol. Cell **62**, 668 (2016).

[6] M. Spielmann, D. G. Lupiáñez, and S. Mundlos, Structural variation in the 3D genome, Nat. Rev. Genet. **19**, 453 (2018).

[7] D. G. Lupiáñez, K. Kraft, V. Heinrich, P. Krawitz, F. Brancati, E. Klopocki, D. Horn, H. Kayserili, J. M. Opitz, R. Laxova, F. Santos-Simarro, B. Gilbert-Dussardier, L. Wittler, M. Borschiwer, S. A. Haas, M. Osterwalder, M. Franke, B. Timmermann, J. Hecht, M. Spielmann, A. Visel, and S.

Mundlos, Disruptions of topological chromatin domains cause pathogenic rewiring of gene-enhancer interactions, Cell **161**, 1012 (2015).

[8] E. Lieberman-Aiden, N. L. Van Berkum, L. Williams, M. Imakaev, T. Ragoczy, A. Telling, I. Amit, B. R. Lajoie, P. J. Sabo, M. O. Dorschner, R. Sandstrom, B. Bernstein, M. A. Bender, M. Groudine, A. Gnirke, J. Stamatoyannopoulos, L. A. Mirny, E. S. Lander, and J. Dekker, Comprehensive mapping of long-range interactions reveals folding principles of the human genome, Science **326**, 289 (2009).

[9] R. A. Beagrie, A. Scialdone, M. Schueler, D. C. A. Kraemer, M. Chotalia, S. Q. Xie, M. Barbieri, I. De Santiago, L. M. Lavitas, M. R. Branco, J. Fraser, J. Dostie, L. Game, N. Dillon, P. A. W. Edwards, M. Nicodemi, and A. Pombo, Complex multi-enhancer contacts captured by genome architecture mapping, Nature (London) **543**, 519 (2017).

[10] S. A. Quinodoz, N. Ollikainen, B. Tabak, A. Palla, J. M. Schmidt, E. Detmar, M. M. Lai, A. A. Shishkin, P. Bhat, Y. Takei, V. Trinh, E. Aznauryan, P. Russell, C. Cheng, M. Jovanovic, A. Chow, L. Cai, P. McDonel, M. Garber, and M. Guttman, Higher-order inter-chromosomal hubs shape 3d genome organization in the nucleus, Cell **174**, 744 (2018).

[11] S. S. P. Rao, M. H. Huntley, N. C. Durand, E. K. Stamenova, I. D. Bochkov, J. T. Robinson, A. L. Sanborn, I. Machol, A. D. Omer, E. S. Lander, and E. L. Aiden, A 3D map of the human genome at kilobase resolution reveals principles of chromatin looping, Cell **159**, 1665 (2014).

[12] E. P. Nora, B. R. Lajoie, E. G. Schulz, L. Giorgetti, I. Okamoto, N. Servant, T. Piolot, N. L. Van Berkum, J. Meisig, J. Sedat, J. Gribnau, E. Barillot, N. Blüthgen, J. Dekker, and E. Heard, Spatial partitioning of the regulatory landscape of the X-inactivation centre, Nature (London) **485**, 381 (2012).

[13] J. R. Dixon, S. Selvaraj, F. Yue, A. Kim, Y. Li, Y. Shen, M. Hu, J. S. Liu, and B. Ren, Topological domains in mammalian genomes identified by analysis of chromatin interactions, Nature (London) **485**, 376 (2012).

[14] J. Fraser, C. Ferrai, A. M. Chiariello, M. Schueler, T. Rito, G. Laudanno, M. Barbieri, B. L. Moore, D. C. Kraemer, S. Aitken, S. Q. Xie, K. J. Morris, M. Itoh, H. Kawaji, I. Jaeger, Y. Hayashizaki, P. Carninci, A. R. Forrest, C. A. Semple, J. Dostie, A. Pombo, and M. Nicodemi, Hierarchical folding and reorganization of chromosomes are linked to transcriptional changes in cellular differentiation, Mol. Syst. Biol. **11**, 852 (2015).

[15] B. van Steensel and A. S. Belmont, Lamina-associated domains: Links with chromosome architecture, heterochromatin, and gene repression, Cell **169**, 780 (2017).

[16] S. Sarnataro, A. M. Chiariello, A. Esposito, A. Prisco, and M. Nicodemi, Structure of the human chromosome interaction network, PLoS One **12**, e0188201 (2017).

[17] T. Nagano, Y. Lubling, T. J. Stevens, S. Schoenfelder, E. Yaffe, W. Dean, E. D. Laue, A. Tanay, and P. Fraser, Single-cell Hi-C reveals cell-to-cell variability in chromosome structure, Nature (London) **502**, 59 (2013).

[18] I. M. Flyamer, J. Gassler, M. Imakaev, H. B. Brandão, S. V. Ulianov, N. Abdennur, S. V. Razin, L. A. Mirny, and K. Tachibana-Konwalski, Single-nucleus Hi-C reveals unique chromatin reorganization at oocyte-to-zygote transition, Nature (London) **544**, 110 (2017).

[19] T. J. Stevens, D. Lando, S. Basu, L. P. Atkinson, Y. Cao, S. F. Lee, M. Leeb, K. J. Wohlfahrt, W. Boucher, A. O'Shaughnessy-Kirwan, J. Cramard, A. J. Faure, M. Ralser, E. Blanco, L. Morey, M. Sansó, M. G. S. Palayret, B. Lehner, L. Di Croce, A. Wutz, B. Hendrich, D. Klenerman, and E. D. Laue, 3D structures of individual mammalian genomes studied by single-cell Hi-C, Nature (London) **544**, 59 (2017).

[20] T. Nagano, Y. Lubling, C. Várnai, C. Dudley, W. Leung, Y. Baran, N. Mendelson Cohen, S. Wingett, P. Fraser, and A. Tanay, Cell-cycle dynamics of chromosomal organization at single-cell resolution, Nature (London) **547**, 61 (2017).

[21] A. N. Boettiger, B. Bintu, J. R. Moffitt, S. Wang, B. J. Beliveau, G. Fudenberg, M. Imakaev, L. A. Mirny, C. Wu, and X. Zhuang, Super-resolution imaging reveals distinct chromatin folding for different epigenetic states, Nature (London) **529**, 418 (2016).

[22] B. Bintu, L. J. Mateo, J.-H. Su, N. A. Sinnott-Armstrong, M. Parker, S. Kinrot, K. Yamaya, A. N. Boettiger, and X. Zhuang, Super-resolution chromatin tracing reveals domains and cooperative interactions in single cells, Science **362**, eaau1783 (2018).

[23] A. M. Cardozo Gizzi, D. I. Cattoni, J.-B. Fiche, S. M. Espinola, J. Gurgo, O. Messina, C. Houbron, Y. Ogiyama, G. L. Papadopoulos, G. Cavalli, M. Lagha, and M. Nollmann, Microscopy-based chromosome conformation capture enables simultaneous visualization of genome organization and transcription in intact organisms, Mol. Cell **74**, 212 (2019).

[24] E. H. Finn, G. Pegoraro, H. B. Brandão, A. L. Valton, M. E. Oomen, J. Dekker, L. Mirny, and T. Misteli, Extensive heterogeneity and intrinsic variation in spatial genome organization, Cell **176**, 1502 (2019).

[25] A. L. Sanborn, S. S. P. Rao, S.-C. Huang, N. C. Durand, M. H. Huntley, A. I. Jewett, I. D. Bochkov, D. Chinnappan, A. Cutkosky, J. Li, K. P. Geeting, A. Gnirke, A. Melnikov, D. McKenna, E. K. Stamenova, E. S. Lander, and E. L. Aiden, Chromatin extrusion explains key features of loop and domain formation in wild-type and engineered genomes, Proc. Natl. Acad. Sci. **112**, E6456 (2015).

[26] G. Fudenberg, M. Imakaev, C. Lu, A. Goloborodko, N. Abdennur, and L. A. Mirny, Formation of chromosomal domains by loop extrusion, Cell Rep. **15**, 2038 (2016).

[27] C. A. Brackley, S. Taylor, A. Papantonis, P. R. Cook, and D. Marenduzzo, Nonspecific bridging-induced attraction drives clustering of DNA-binding proteins and genome organization, Proc. Natl. Acad. Sci. USA **110**, E3605 (2013).

[28] D. Jost, P. Carrivain, G. Cavalli, and C. Vaillant, Modeling epigenome folding: formation and dynamics of topologically associated chromatin domains, Nucleic. Acids. Res. **42**, 9553 (2014).

[29] M. Bohn and D. W. Heermann, Diffusion-driven looping provides a consistent framework for chromatin organization, PLoS One **5**, e12218 (2010).

[30] M. Nicodemi and A. Prisco, Thermodynamic pathways to genome spatial organization in the cell nucleus, Biophys. J. **96**, 2168 (2009).

[31] M. Barbieri, M. Chotalia, J. Fraser, L.-M. Lavitas, J. Dostie, A. Pombo, and M. Nicodemi, Complexity of chromatin folding is captured by the strings and binders switch model, Proc. Natl. Acad. Sci. **109**, 16173 (2012).

[32] M. Di Pierro, B. Zhang, E. L. Aiden, P. G. Wolynes, and J. N. Onuchic, Transferable model for chromosome architecture, Proc. Natl. Acad. Sci. **113**, 12168 (2016).

[33] A. Buckle, C. A. Brackley, S. Boyle, D. Marenduzzo, and N. Gilbert, Polymer simulations of heteromorphic chromatin pre-

dict the 3d folding of complex genomic loci, Mol. Cell **72**, 786 (2018).
[34] G. Shi, L. Liu, C. Hyeon, and D. Thirumalai, Interphase human chromosome exhibits out of equilibrium glassy dynamics, Nat. Commun. **9**, 3161 (2018).
[35] A. M. Chiariello, C. Annunziatella, S. Bianco, A. Esposito, and M. Nicodemi, Polymer physics of chromosome large-scale 3D organisation, Sci. Rep. **6**, 29775 (2016).
[36] A. M. Chiariello, S. Bianco, A. M. Oudelaar, A. Esposito, C. Annunziatella, L. Fiorillo, M. Conte, A. Corrado, A. Prisco, M. S. C. Larke, J. M. Telenius, R. Sciarretta, F. Musella, V. J. Buckle, D. R. Higgs, J. R. Hughes, and M. Nicodemi, A dynamic folded hairpin conformation is associated with α-globin activation in erythroid cells, Cell Rep. **30**, 2125 (2020).
[37] M. Conte, L. Fiorillo, S. Bianco, A. M. Chiariello, A. Esposito, and M. Nicodemi, Polymer physics indicates chromatin folding variability across single-cells results from state degeneracy in phase separation, Nat. Commun. **11**, 3289 (2020).
[38] S. Bianco, D. G. Lupiáñez, A. M. Chiariello, C. Annunziatella, K. Kraft, R. Schöpflin, L. Wittler, G. Andrey, M. Vingron, A. Pombo, S. Mundlos, and M. Nicodemi, Polymer physics predicts the effects of structural variants on chromatin architecture, Nat. Genet. **50**, 662 (2018).
[39] N. Naumova, M. Imakaev, G. Fudenberg, Y. Zhan, B. R. Lajoie, L. A. Mirny, and J. Dekker, Organization of the mitotic chromosome, Science **342**, 948 (2013).
[40] T. Sexton, E. Yaffe, E. Kenigsberg, F. Bantignies, B. Leblanc, M. Hoichman, H. Parrinello, A. Tanay, and G. Cavalli, Three-dimensional folding and functional organization principles of the drosophila genome, Cell **148**, 458 (2012).
[41] Z. Duan, M. Andronescu, K. Schutz, S. McIlwain, Y. J. Kim, C. Lee, J. Shendure, S. Fields, C. A. Blau, and W. S. Noble, A three-dimensional model of the yeast genome, Nature (London) **465**, 363 (2010).
[42] F. Benedetti, J. Dorier, Y. Burnier, and A. Stasiak, Models that include supercoiling of topological domains reproduce several known features of interphase chromosomes, Nucleic Acids. Res. **42**, 2848 (2014).
[43] R. Kalhor, H. Tjong, N. Jayathilaka, F. Alber, and L. Chen, Genome architectures revealed by tethered chromosome conformation capture and population-based modeling, Nat. Biotechnol. **30**, 90 (2012).
[44] A. Yu. Grosberg, S. K. Nechaev, and E. I. Shakhnovich, The role of topological constraints in the kinetics of collapse of macromolecules, J. Phys. France **49**, 2095 (1988).
[45] L. A. Mirny, The fractal globule as a model of chromatin architecture in the cell, Chromosome Res. **19**, 37 (2011).
[46] R. D. Schram, G. T. Barkema, and H. Schiessel, On the stability of fractal globules, J. Chem. Phys. **138**, 224901 (2013).
[47] M. Nicodemi and A. Pombo, Models of chromosome structure, Curr. Opin. Cell Biol. **28**, 90 (2014).
[48] B. Bonev, N. Mendelson Cohen, Q. Szabo, L. Fritsch, G. L. Papadopoulos, Y. Lubling, X. Xu, X. Lv, J. P. Hugnot, A. Tanay, and G. Cavalli, Multiscale 3D genome rewiring during mouse neural development, Cell **171**, 557 (2017).
[49] P. G. De Gennes, *Scaling Concepts in Polymer Physics* (Cornell University Press, Ithaca, NY, 1979).
[50] K. Kremer and G. S. Grest, Dynamics of entangled linear polymer melts: A molecular-dynamics simulation, J. Chem. Phys. **92**, 5057 (1990).
[51] S. Plimpton, Fast parallel algorithms for short-range molecular dynamics, J. Comput. Phys. **117**, 1 (1995).
[52] M. Doi and S. F. Edwards, *The Theory of Polymer Dynamic* (Oxford Science Publications, Clarendon Press, Oxford, 1986).
[53] C. Annunziatella, A. M. Chiariello, A. Esposito, S. Bianco, L. Fiorillo, and M. Nicodemi, Molecular dynamics simulations of the strings and binders switch model of chromatin, Methods **142**, 81 (2018).
[54] A. Rosa and R. Everaers, Structure and dynamics of interphase chromosomes, PLoS Comput. Biol. **4**, e1000153 (2008).
[55] D. Hnisz, K. Shrinivas, R. A. Young, A. K. Chakraborty, and P. A. Sharp, A phase separation model for transcriptional control, Cell **169**, 13 (2017).
[56] B. R. Sabari, A. Dall'Agnese, A. Boija, I. A. Klein, E. L. Coffey, K. Shrinivas, B. J. Abraham, N. M. Hannett, A. V. Zamudio, J. C. Manteiga, C. H. Li, Y. E. Guo, D. S. Day, J. Schuijers, E. Vasile, S. Malik, D. Hnisz, T. I. Lee, I. I. Cisse, R. G. Roeder, P. A. Sharp, A. K. Chakraborty, and R. A. Young, Coactivator condensation at super-enhancers links phase separation and gene control, Science **361**, eaar3958 (2018).
[57] R. Cortini and G. J. Filion, Theoretical principles of transcription factor traffic on folded chromatin, Nat. Commun. **9**, 1740 (2018).
[58] W.-K. Cho, J.-H. Spille, M. Hecht, C. Lee, C. Li, V. Grube, and I. I. Cisse, Mediator and RNA polymerase II clusters associate in transcription-dependent condensates, Science **361**, 412 (2018).
[59] A. M. Chiariello, F. Corberi, and M. Salerno, The interplay between phase separation and gene-enhancer communication: A theoretical study, Biophys. J. **119**, 873 (2020).
[60] C. Annunziatella, A. M. Chiariello, S. Bianco, and M. Nicodemi, Polymer models of the hierarchical folding of the Hox-B chromosomal locus, Phys. Rev. E **94**, 042402 (2016).
[61] S. Shinkai, M. Nakagawa, T. Sugawara, Y. Togashi, H. Ochiai, R. Nakato, Y. Taniguchi, and S. Onami, PHi-C: deciphering Hi-C data into polymer dynamics, NAR Genomics Bioinforma **2**, lqaa020 (2020).
[62] S. Shinkai, T. Nozaki, K. Maeshima, and Y. Togashi, Dynamic nucleosome movement provides structural information of topological chromatin domains in living human cells, PLOS Comput. Biol. **12**, e1005136 (2016).
[63] C. A. Brackley, J. M. Brown, D. Waithe, C. Babbs, J. Davies, J. R. Hughes, V. J. Buckle, and D. Marenduzzo, Predicting the three-dimensional folding of cis-regulatory regions in mammalian genomes using bioinformatic data and polymer models, Genome Biol. **17**, 59 (2016).
[64] Y. Shin and C. P. Brangwynne, Liquid phase condensation in cell physiology and disease, Science **357**, eaaf4382 (2017).
[65] Y. Shin, Y.-C. Chang, D. S. W. Lee, J. Berry, D. W. Sanders, P. Ronceray, N. S. Wingreen, M. Haataja, and C. P. Brangwynne, Liquid nuclear condensates mechanically sense and restructure the genome, Cell **175**, 1481 (2018).
[66] G. Ponti, F. Palombi, D. Abate, F. Ambrosino, G. Aprea, T. Bastianelli, F. Beone, R. Bertini, G. Bracco, M. Caporicci, B. Calosso, M. Chinnici, A. Colavincenzo, A. Cucurullo, P. Dangelo, M. De Rosa, P. De Michele, A. Funel, G. Furini, D. Giammattei, S. Giusepponi, R. Guadagni, G. Guarnieri, A. Italiano, S. Magagnino, A. Mariano, G. Mencuccini, C. Mercuri, S. Migliori, P. Ornelli, S. Pecoraro, A. Perozziello, S. Pierattini, S. Podda, F. Poggi, A. Quintiliani, A. Rocchi, C.

Scio, F. Simoni, and A. Vita, The Role of Medium Size Facilities in the HPC Ecosystem: The Case of the New CRESCO4 Cluster Integrated in the ENEAGRID Infrastructure, in *Proceedings of the 2014 International Conference on High Performance Computing and Simulation, HPCS 2014* (IEEE, 2014), pp. 1030–1033.